Magnetic Ordering in Chiral Nanotubes with Competing Interactions

Author: Itxaso Muñoz-Aldalur, itxaso.mam@gmail.com
Dpt. Física de la Matèria Condensada, Facultat de Física, Universitat de Barcelona, Diagonal 645, 08028 Barcelona, Spain.

Advisor: Òscar Iglesias Clotas, oscariglesias@ub.edu

Abstract: In this work, we investigate the low-temperature equilibrium magnetic configurations of single-wall magnetic nanotubes with competing exchange and dipolar interactions using Monte Carlo simulations within the framework of the classical 3D Heisenberg model. The nanotubes are constructed by folding planar spin lattices at various chiral angles, allowing control over radius, length, and underlying lattice. Through the analysis of the different magnetization components and energies, we have revealed a rich variety of stable magnetic states, including uniform, vortex-like, and helical configurations, whose nature strongly depends on the tube aspect ratio, length, chirality, and the ratio $\gamma = g/J$. The inclusion of anisotropy further enriches the phase space, stabilizing radial and mixed magnetization textures. These findings highlight the crucial role of geometry and interaction competition in chiral nanomagnets and provide insight into the design of functional magnetic nanostructures. **Keywords:** Magnetic nanotubes, magnetic configurations, chiral magnetism, anisotropy, Heisenberg model, MC simulation. **SDGs:** 4, 6 & 9.

I. INTRODUCTION

Magnetic nanotubes offer a versatile platform for exploring both fundamental and applied aspects of nanomagnetism. Their cylindrical geometry enables the investigation of curvature-driven magnetic phenomena, extending beyond the behavior observed in flat thin films [1]. Advances in synthesis and characterization have enabled a shift from ensemble measurements to single-object studies, deepening our understanding of magnetization reversal, domain wall dynamics, and magnetic anisotropy [2]. This interaction interplay can lead to a rich variety of magnetic ground states, highly influenced by the tube's chiral structure. Magnetic configurations are key to designing functional nanostructures with tunable electronic, optoelectronic, and mechanical properties. Potential applications include sensors, logic devices [3], high-density magnetic memories [4], magnetic hyperthermia and controlled drug delivery [5].

Single-wall nanotubes (NTs) are remarkable one-dimensional structures formed by rolling two-dimensional sheets according to a chiral vector $\vec{C}$ and with a periodicity defined by a translational vector $\vec{T}$ (see Fig. 1a for a sketch of the geometry). The chiral vector, which dictates the twist direction of the NT, is defined in terms of the unit vectors of the original lattice $\vec{a_1}, \vec{a_2}$ (forming an angle φ) as

$$\vec{C} = n\vec{a_1} + m\vec{a_2}, \tag{1}$$

where n and m are integers (chiral indices). Its length determines the NT radius $R = |\vec{C}|/2\pi$. Furthermore, the translational vector given by

$$\vec{T} = x\vec{a_1} - y\vec{a_2}\,, \tag{2}$$

determines the periodicity along the tube axis and its length. The chiral vector and the chiral angle ($\angle(\vec{C}, \vec{a}_1)$) are crucial to determine the magnetic and electronic properties of NTs [6]. Our study will focus on three relevant tube types, which will be denoted: AA ($\varphi = \pi/2$, n or $m = 0$, formed by equally spaced rings with nodes forming columns), AB ($\varphi = \pi/3$, n or $m = 0$, with an underlying triangular lattice) and Zigzag (ZZ) ($\varphi = \pi/2$, $n = m$, formed by stacked and twisted rings).

II. MODEL AND SIMULATION DETAILS

Our model is based on 3D Heisenberg spins $\vec{S}$ placed at the nodes of the NT lattice and interacting through the following Hamiltonian [7]

$$\hat{H} = E_{ex} + E_{dip} + E_{ani}, \tag{3}$$

where E_{ex} is the short-range exchange coupling between nearest neighbors,

$$E_{ex} = -\sum_{\langle i,j \rangle} J_{ij} \vec{S_i} \cdot \vec{S_j}, \tag{4}$$

with $J_{ij} = J > 0$, the ferromagnetic (FM) exchange constant. The second term is the long-range magnetic dipolar interaction

$$E_{dip} = g \sum_{i<j} \frac{\vec{S_i} \cdot \vec{S_j} - 3(\vec{S_i} \cdot \hat{r}_{ij})(\vec{S_j} \cdot \hat{r}_{ij})}{|\vec{r_{ij}}|^3}, \tag{5}$$

where g is the dipolar coupling constant, $\vec{r_{ij}}$ the relative distance between i and j spins and the sum is for all (i, j) pairs. From now on, we establish $J = 1$ and define the dimensionless parameter $\gamma = g/J$ as the ratio between both interactions.

In the second part of our study, we will add a third term that accounts for magnetocrystalline uniaxial anisotropy [8]

$$E_{ani} = -K \sum_{i}^{N} (\vec{S}_i \cdot \vec{n}_i)^2 \tag{6}$$

where K is the anisotropy constant and $\vec{n}_i$ the local easy-axes.

We have used a self-made FORTRAN Monte Carlo (MC) code that uses the Metropolis algorithm to flip one spin at a time. The low temperature equilibrium magnetic configurations are obtained after an annealing process starting from high enough temperatures and a random spin configuration (see [9] for the code files and structure, and additional simulation details).

In order to characterize the equilibrium configurations, we have found it convenient to use the total magnetization components in cylindrical coordinates, which we will also use as the order parameters determining the different magnetic phases. This was achieved by projecting the spin vectors onto a local coordinate system defined at each spin position $\vec{r}_i = (R\cos\alpha_i, R\sin\alpha_i, z_i)$ ($\alpha_i = \arctan(y_i/x_i)$ being the angular position). With this, the cylindrical spin components have been calculated from the polar and azimuthal angles θ_i and φ_i extracted from the output simulation data as

$$\begin{cases} s_{\rho i} = \sin\theta_i \cos(\varphi_i - \alpha_i) \\ s_{\varphi i} = \sin\theta_i \sin(\varphi_i - \alpha_i) \\ s_{zi} = \cos\theta_i . \end{cases} \qquad \begin{cases} m_\rho = \frac{1}{N}\sum_{i=1}^{N} |s_{\rho i}| \\ m_\varphi = \frac{1}{N}\sum_{i=1}^{N} |s_{\varphi i}| \\ m_z = \frac{1}{N}\sum_{i=1}^{N} |s_{zi}| . \end{cases} \tag{7}$$

With m_ρ, m_φ, m_z the average magnetization components.

III. RESULTS

A. Nanotubes with only dipolar interactions

We will start by studying NTs with only dipolar interactions ($g = 1, J = 0$) as in this case it is well known that the spatial arrangement of the spins influences the kind of magnetic order [10], due to the long range of the dipolar interactions. Taking as a reference the case studied in [7], we have considered three NT types with the same dimensions (8×29). The obtained configurations are presented in Fig. 1c, where snapshots of the unfolded NT have been included for the sake of clarity.

For the AA tube, the dipolar interaction favors a FM alignment of the spins along the tube length, with antiferromagnetic (AFM) order between spin columns, and microvortices forming at the NT ends that favor flux closure due to finite-size effects. In contrast, the equilibrium state of AB NTs, whose underlying lattice is triangular, is a vortex configuration with all spins aligning tangentially to the cylinder and perpendicular to the NT axis. Finally, for the ZZ NTs, the equilibrium state can be characterized as antiferromagnetic helical (AH) order. This is because the distance between spins in different rings is shorter than that between those in the same ring. The spins align head-to-tail along helices that follow the n.n. directions, which are AFM coupled between them (diagonal AFM stripes in the unfolded representation).

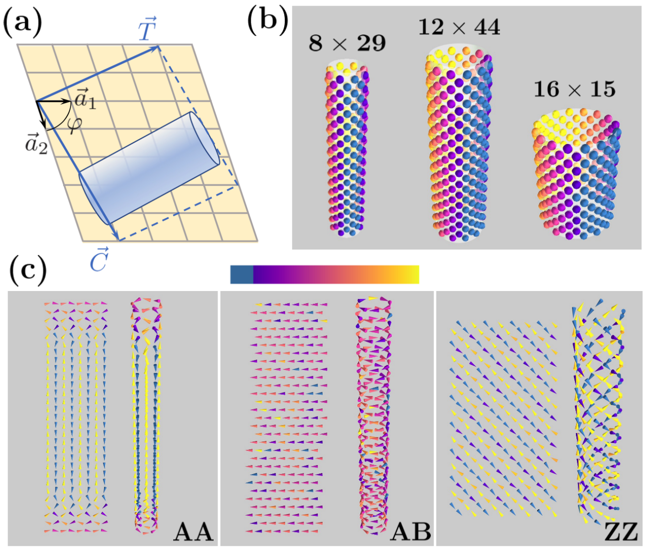

FIG. 1: (a) Schematic of a generic Bravais planar lattice and its folding into NT following the chiral vector $\vec{C}$ direction. (b) Examples of the studied NTs with spheres representing the spins positions and sizes as indicated. (c) Magnetic equilibrium configurations of the 8×29 NTs with dipolar interactions only, shown for the three NT types. Unfolded planar representations of each configuration are also included.

B. Nanotubes with competing interactions

The next part of our study aims to determine how the competition between short-range (exchange) and long-range (dipolar) interactions influences the low-temperature magnetic order of the NT. As an extension of previous work [7], we have considered the three NT types with three sizes each, as shown in Fig. 1: two with high and one with low aspect ratio. We have run simulations for a wide range of γ values and plotted the cylindrical total magnetization components of the equilibrium configurations for all nine cases in Fig. 2 together with some representative snapshots.

Two general features are common to all NT types and dimensions within the range of γ presented in that figure: a) the spins are tangential to the tube surface, as indicated by the vanishing values of m_ρ; b) there is a transition from FM states with $m_z \approx 1, m_\varphi \approx 0$ for $\gamma = 0$ to V states with $m_\varphi \approx 1, m_z \approx 0$ as γ increases. For intermediate γ values, mixed configurations emerge whose details depend on the tube type and will be analyzed in what follows. In particular, ZZ type NTs form helicoidal (H) states, characterized by a FM core region whose length decreases when increasing γ, and vortices at the tube

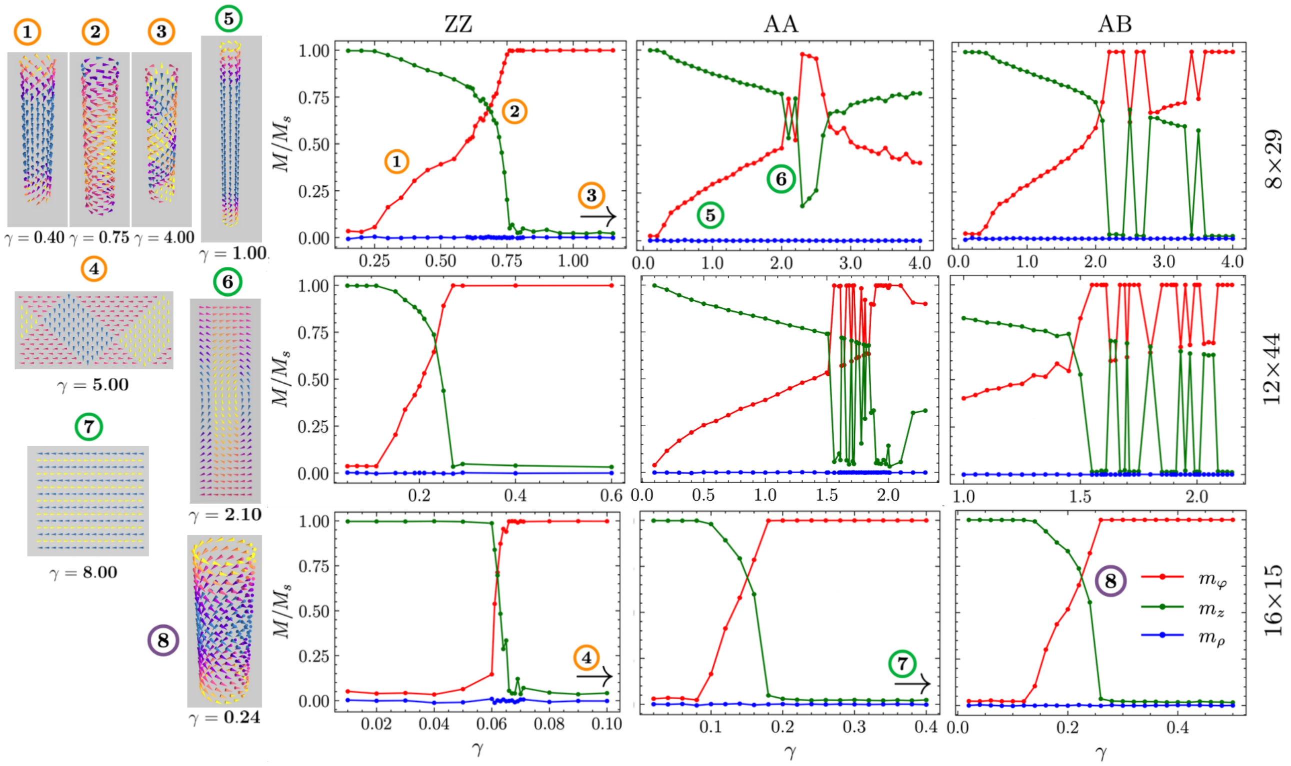

FIG. 2: Cylindrical components of the normalized NT magnetization (m_φ, m_z, m_ρ) of the equilibrium configurations obtained by simulated annealing as a function of $\gamma = g/J$. Magnetic anisotropy is not taken into account. Results are shown for the three NT types studied (ZZ, AA and AB) and three representative sizes as indicated in the main panels. In the left panels, snapshots of some representative configurations mentioned in Table I are displayed. For better visibility, zoomed out versions have been included in Appendix A.

ends (see the snapshot (1) in Fig. 2), until the FM core region disappears (see the snapshot (2) in Fig. 2). These H states result from the competition between exchange interactions, which favor axial FM alignment, and dipolar interactions, which promote states with higher vorticity around the NT axis. As either the NT length or radius increases, the onset of the H states shifts to lower γ values, and its stability range becomes narrower. For NTs with low aspect ratios, the transition from FM to V states is more abrupt, as the two vortices at the tube ends in an H state occupy a larger fraction of the total NT length (snapshot (8) in Fig. 2).

For AA and AB type NTs with high aspect ratios, mixed magnetic states emerge even at small γ values and persist across a broad range, extending up to $\gamma = 2, 1.5$ for tubes with dimensions $8 \times 29, 12 \times 44$, respectively. Compared to ZZ NTs, the axial and azimuthal magnetization components of the H states exhibit a more gradual linear decrease and increase, respectively (as shown in the AA and AB panels for the 8×29 and 12×44 sizes in Fig. 2, illustrated with examples in the (5) and (6) snapshots). The fluctuations in the magnetization components of the equilibrium states observed beyond the range described in the previous paragraph are attributed to the high degree of degeneracy among the V, FM and H states within that γ range. This degeneracy, previously studied in detail for ZZ NTs in [7], makes it particularly challenging to identify the true ground state, even when increasing the number of MC steps in the simulation.

The curvature introduced when rolling a planar lattice into a cylindrical surface, combined with the finite size of the NTs, partially explains the observed degeneracy, an effect that would be absent in planar geometries such as thin films. Notice also that the extent of the metastability region is more pronounced in AB type NTs than in AA type ones, due to differences in their underlying lattices. While AA tubes are formed by folding a square lattice, AB tubes' spins exhibit triangular spins coordination, which introduces geometrical frustration in the dipolar interactions and promotes the appearance of energetically degenerate states.

On the other hand, NTs with small aspect ratio (bottom-row panels in Fig. 2) do not exhibit this metastability phenomenon. In these cases, the dipolar-induced shape anisotropy perpendicular to the tube axis dominates over the exchange interaction as soon as the mixed H region is surpassed.

When increasing γ beyond the values considered in Fig. 2, dipolar interactions begin to dominate over exchange, and the equilibrium states should tend to approach those for purely dipolar NTs, presented in Sec. III A. Although not shown due to space limitations,

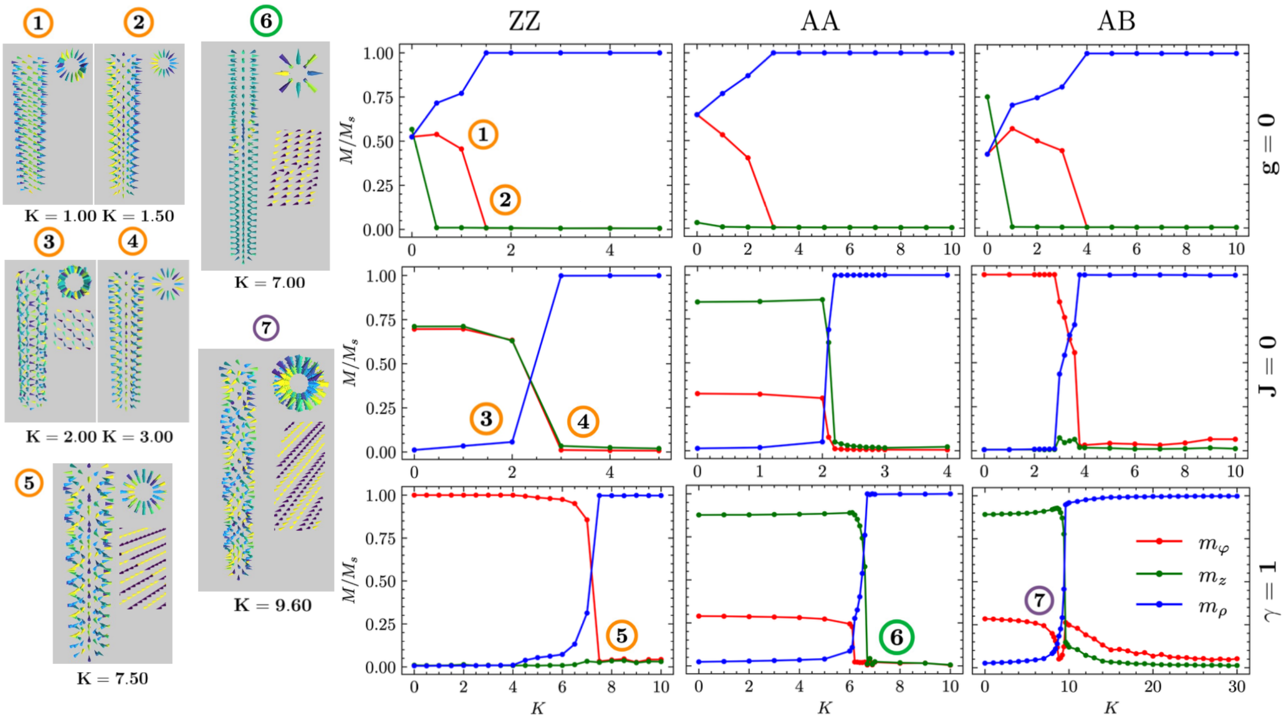

FIG. 3: Cylindrical components of the normalized NT magnetization (m_φ, m_z, m_ρ) of the equilibrium configurations obtained by simulated annealing as a function of $\gamma = g/J$. Radial magnetic anisotropy has been included here. Results are shown for NTs of dimensions 8×29 and three NT types studied (ZZ, AA and AB). Each row corresponds to cases with only exchange $(g = 0)$, only dipolar $(J = 0)$, and both interactions present $(\gamma = 1)$. Snapshots of some representative configurations mentioned in Table I are displayed in the left panels with labels that identify the region in the main panels. For better visibility, zoomed out versions have been included in Appendix A.

we have confirmed that this transition indeed occurs for both ZZ and AA type NTs. In these cases, a new transition region appears at high γ: around $4 < \gamma < 8$ for ZZ and 8×29 AA, with lower thresholds for larger tubes (see Tab. I), in which a sequence of complex states emerges.

These include AFM ordered stripe patterns of decreasing width (snapshot (3) in Fig. 2) and flux closure Landau domains (snapshot (4) in Fig. 2) forming in the central region of the tube. For the small aspect ratio NT, a new AV pattern is formed, also with stripe patterns of decreasing width (snapshot (7) in Fig. 2). These configurations eventually converge to the ground states observed for $J = 0$, where dipolar interactions are solely responsible for the ordering, except for the low ratio tube, which is heavily impacted by the previously mentioned dipolar-induced shape anisotropy.

C. Nanotubes with radial anisotropy

In planar thin films and other two-dimensional magnetic systems, the magnetocrystalline anisotropy often favors magnetization perpendicular to the film surface. When such a film is rolled into a cylindrical NT, this anisotropy translates into a radial configuration, with local easy axes oriented normally to the tube surface. Therefore, in this last section, we explore the impact of magnetocrystalline anisotropy on the equilibrium configurations by incorporating the corresponding energy term from Eq. 6. We will consider again the three types of NT, restricting the analysis to tubes with dimensions 8×29. Also, three possible scenarios: 1) NTs with only exchange interaction ($J = 1$, fixing $g = 0$); 2) NTs with only dipolar interaction ($J = 0$, fixing $g = 1$); 3) competing exchange and dipolar interaction present (fixing $\gamma = 1$). For each case, we performed simulations over a range of anisotropy strengths K, and extracted the cylindrical components of the total magnetization of the equilibrium configurations. These results are presented in Fig. 3, which also includes representative snapshots that illustrate the characteristic states induced by varying K.

In the case where only exchange is considered, we have previously shown that the equilibrium configurations when $K = 0$ are FM for all NT types, with no preferred orientation due to the absence of anisotropy. The introduction of anisotropy breaks this degeneracy, favoring spin alignment along the basal plane of the NT. As K increases, a gradual reorientation of the spins towards the local radial direction occurs, reflected by the increase in the m_ρ component. This leads to the formation of flower radial states, analogous to those observed in ring- or disk-shaped nanomagnets with in-plane anisotropy (see snapshot (1) in Fig. 3). Beyond a critical anisotropy value K_c, fully radial FM configurations (with $m_\rho = 1, m_{\varphi,z} = 0$) are stabilized for all tube types (see snapshot (2) in Fig. 3). The precise value of K_c depends on the tube type.

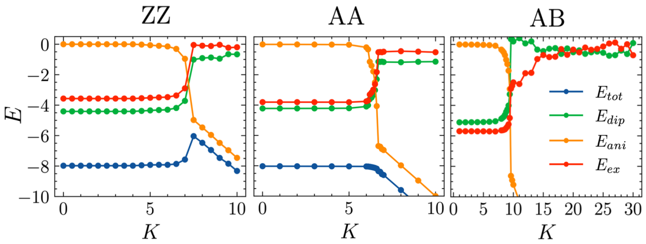

FIG. 4: Total energies and their separate contributions as a function of the anisotropy constant K, for $\gamma = 1$. The transition where anisotropic energy dominates (complete radial state) is different for the three kinds of NTs: $K \sim 7, 6.7, 9.6$, for ZZ, AA and AB tubes, respectively.

For dipolar-only interactions ($J = 0$, $g = 1$), initial configurations at $K = 0$ strongly differ across NT types, as already discussed in Sec. III A. Above critical anisotropy K_c, all systems transition to now radial AFM states with geometry-dependent patterns: AFM-coupled rings (ZZ) (snapshot (4) in Fig. 3), checkerboard-like AFM pattern (AA), and frustrated AFM configurations (AB) due to triangular coordination. These transitions occur through complex intermediate states within narrow K windows, varying within NT types. An illustrative example for the ZZ NT is snapshot (3) of Fig. 3, where the emergence of micro-vortices precedes the final radial reorientation. AA NTs show end-to-center radial AFM opening propagation, gradually destabilizing the longitudinal AFM core until it vanishes around $K \approx 2.5$. In AB NTs, spins begin to tilt radially across all rings almost simultaneously, leading to ringwise radial AFM states that fully develop around $K \approx 3.4$.

At $\gamma = 1$, anisotropy-induced transitions start from different configurations: V-like states for ZZ NTs, and hybrid FM+V states for AA and AB NTs (see lower panels in Fig. 3). All evolve toward radial AFM configurations with patterns determined by the underlying lattice geometry. In ZZ NTs, anisotropy gradually destabilizes the V configuration. For $K \gtrsim 7.0$, spins begin to rotate radially from the tube ends, creating mixed states where radial FM and AFM domains coexist in spatially disordered patterns due to the competing interactions and geometric constraints ((5) in Fig. 3). In AA NTs, the transition resembles the $J = 0$ case but exchange delays radial AFM onset. Starting from central FM alignment, radial AFM ordering develops at the ends and propagates inward. Complete transformation to a mixed radial state occurs around $K \approx 6.7$, with domain-like irregularities appearing at higher anisotropy ((6) in Fig. 3). In AB NTs, triangular lattice frustration creates more complex behavior. Around $K \approx 9.6$, helically modulated radial AFM stripes form with two-spin periodicity ((7) in Fig. 3). Further increasing K produces frustrated radial states with coexisting radial FM and radial AFM domains, similar to the $J = 0$ case but with stronger lattice-induced frustration.

Energy decomposition (Fig. 4) reveals that the anisotropy threshold for radial state formation is directly controlled by the underlying tube geometry, providing a clear structure-property relationship.

IV. CONCLUSIONS

Our study has shown that the competition between short-range exchange and long-range dipolar interactions gives rise to a diverse variety of magnetic configurations, depending on the folding, chiral vector and size of the NTs. We have extended previous studies focused on ZZ NTs to other NT types, identifying key magnetic transitions: FM → V → AH in ZZ tubes, FM+V → AFM+V in AA tubes, and FM → V in AB tubes. Inclusion of radial anisotropy has revealed how exchange favors radial FM while dipolar promotes radial AFM, with frustration emerging in AB tubes when both compete. Tab. I summarizes all results.

We are planning to extend the present study including the chiral Dzyaloshinskii-Moriya interaction to explore the formation of topological structures such as skyrmions in curved magnetic structures [11].

Acknowledgments

Firstly, I would like to thank Dr. Òscar Iglesias for his brilliant guidance, help, and advice. We also acknowledge CSUC for computational resources. Finally, but just as importantly, I want to thank my family and friends for their unwavering support.

[1] K. Yershov *et al.*, Phys. Rev. B **110**, 134428 (2025).
[2] O. Fruchart *et al.*, in *Handbook of Magnetic Materials*, Vol. 27, edited by K. Buschow (Elsevier B.V., 2019) pp. 155–251.
[3] R. P. Cowburn *et al.*, Science **287**, 1466 (2000).
[4] S. S. P. Parkin *et al.*, Science **320**, 190 (2008).
[5] J. Alonso *et al.*, J. Appl. Phys. **117**, 17D113 (2015).
[6] J. M. de Albornoz-Caratozzolo *et al.*, Nanoscale Adv. **6**, 79 (2024).
[7] H. D. Salinas *et al.*, Sci Rep **8**, 10275 (2018).
[8] K. Krishnan, *Fundamentals and applications of magnetic materials* (Oxford University Press, 2016).
[9] I. Muñoz-Aldalur and O. Iglesias, "Github repository," .
[10] I. Stankovic *et al.*, Nanoscale **11**, 2521 (2019).
[11] K. V. Yershov *et al.*, SciPost Phys. **9**, 043 (2020).

Ordenació Magnètica en Nanotubs Quirals amb Interaccions Competitives

Author: Itxaso Muñoz-Aldalur, itxaso.mam@gmail.com
Dpt. Física de la Matèria Condensada, Facultat de Física, Universitat de Barcelona, Diagonal 645, 08028 Barcelona, Spain.

Advisor: Òscar Iglesias Clotas, oscariglesias@ub.edu

Resum: En aquest treball, s'han investigat les configuracions magnètiques d'equilibri a baixa temperatura de nanotubs magnètics d'una sola paret amb la competència d'interaccions d'intercanvi i dipolar, utilitzant simulacions Monte Carlo dins del marc del model clàssic de Heisenberg 3D. Els nanotubs es construeixen plegant xarxes de spins planars amb diversos angles quirals, cosa que permet el control sobre el radi, la longitud i la xarxa subjacent. Mitjançant l'anàlisi de les diferents components de la magnetització i les energies, hem revelat una rica varietat d'estats magnètics estables, incloent-hi configuracions uniformes, de tipus vòrtex i helicoidals, la naturalesa dels quals depèn fortament de la relació d'aspecte del tub, la longitud, la quiralitat i la relació $\gamma = g/J$. La inclusió de l'anisotropia enriqueix encara més l'espai de fases, estabilitzant textures de magnetització radials i mixtes. Aquestes troballes destaquen el paper crucial de la geometria i la competència d'interaccions en nanomagnets quirals i proporcionen una comprensió per al disseny de nanoestructures magnètiques funcionals. **Paraules clau:** Nanotubs magnètics, configuracions magnètiques, magnetisme quiral, anisotropia, model de Heisenberg, simulació Monte Carlo.
ODSs: 4, 6 i 9.

Objectius de Desenvolupament Sostenible (ODSs o SDGs)

1. Fi de les desigualtats		10. Reducció de les desigualtats	
2. Fam zero		11. Ciutats i comunitats sostenibles	
3. Salut i benestar		12. Consum i producció responsables	
4. Educació de qualitat	X	13. Acció climàtica	
5. Igualtat de gènere		14. Vida submarina	
6. Aigua neta i sanejament	X	15. Vida terrestre	
7. Energia neta i sostenible		16. Pau, justícia i institucions sòlides	
8. Treball digne i creixement econòmic		17. Aliança pels objectius	
9. Indústria, innovació, infraestructures	X		

El contingut d'aquest Treball de Fi de Grau (TFG), com a part d'un grau universitari de Física, es relaciona directament amb l'**ODS 4** (Educació de qualitat), especialment amb la fita 4.4, en contribuir a la formació i la recerca en l'àmbit universitari. A més, la investigació fonamental sobre nanotubs magnètics i el desenvolupament de nous materials s'alinea amb l'**ODS 9** (Indústria, innovació i infraestructures), promovent la fita 9.5 relativa a la millora de la recerca científica i les capacitats tecnològiques. Finalment, els avenços en el coneixement dels nanotubs, i en particular dels de carboni, són crucials per al desenvolupament de tecnologies de purificació d'aigua i sanejament, establint una relació amb l'**ODS 6** (Aigua neta i sanejament).

GRAPHICAL ABSTRACT

Magnetic Ordering in Chiral Nanotubes with Competing Interactions

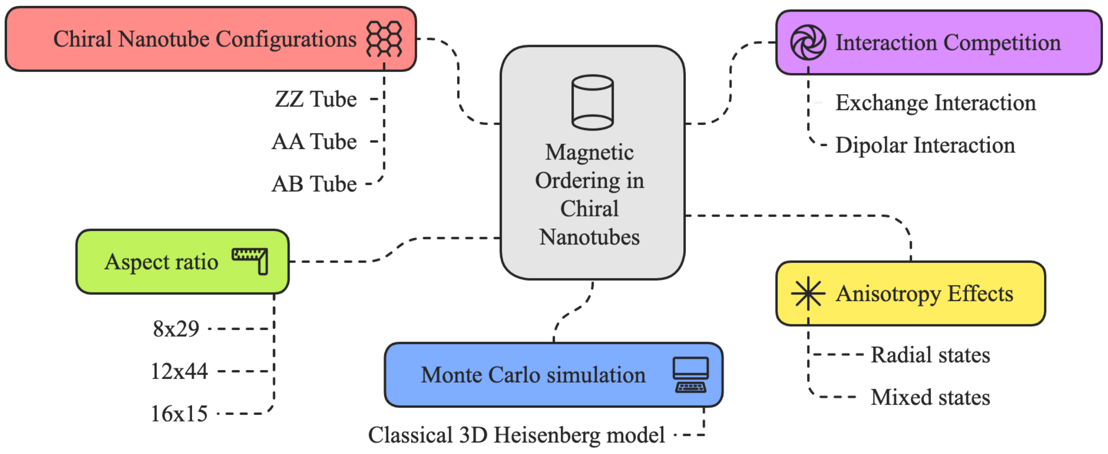

Appendix A: Enlarged representations of characteristic configurations

1. Summary of transitions

TABLE I: Summary of magnetic phase transitions for different system sizes and interaction types. Critical transition points (γ_c or K_c) are indicated. Abbreviations: FM (Ferromagnetic), AFM (Antiferromagnetic), V (Vortex), AH (Antiferromagnetic Helix), AV (Antiferromagnetic Vortex).

System	Interaction	Parameters	Phase Sequence	Critical Points
8×29	**ZZ**	$K = 0, J = 1$	FM → V → mixed AH → AH	$\gamma \sim 0.7, 4.0 - 8.0$
		$K \neq 0, J = 1, g = 0$	FM → radial FM	$K \sim 1.5$
		$K \neq 0, J = 0, g = 1$	AH → radial AFM	$K \sim 2.5$
		$K \neq 0, J = 1, g = 1$	V → mixed radial FM+AFM	$K \sim 7$
	AA	$K = 0, J = 1$	FM → AFM center+V → perfect AFM+V	$\gamma \sim 2.1, 8.0$
		$K \neq 0, J = 1, g = 0$	FM → radial FM	$K \sim 3.0$
		$K \neq 0, J = 0, g = 1$	AFM center+V → radial AH	$K \sim 2.5$
		$K \neq 0, J = 1, g = 1$	FM center+V → radial AFM →mixed	$K \sim 6.7$
	AB	$K = 0, J = 1$	FM → V	$\gamma \sim 2$
		$K \neq 0, J = 1, g = 0$	FM → radial FM	$K \sim 4.0$
		$K \neq 0, J = 0, g = 1$	V → partial radial AFM → frustrated	$K \sim 3.4$
		$K \neq 0, J = 1, g = 1$	FM+V → radial AH → frustrated	$K \sim 9.6$
12×44	**ZZ**	$K = 0, J = 1$	FM → V → mixed AH → AH	$\gamma \sim 0.29, 4.0 - 8.0$
	AA	$K = 0, J = 1$	FM → AFM center+V → perfect AFM+V	$\gamma \sim 1.5 - 2, 8.0$
	AB	$K = 0, J = 1$	FM → V	$\gamma \sim 1.5$
16×15	**ZZ**	$K = 0, J = 1$	FM → V → mixed AH → AH	$\gamma \sim 0.06, 5.0 - 8.5$
	AA	$K = 0, J = 1$	FM → V → variety AV → perfect AV	$\gamma \sim 0.18, 8.5$
	AB	$K = 0, J = 1$	FM → V	$\gamma \sim 0.26$

2. Results with no anisotropy

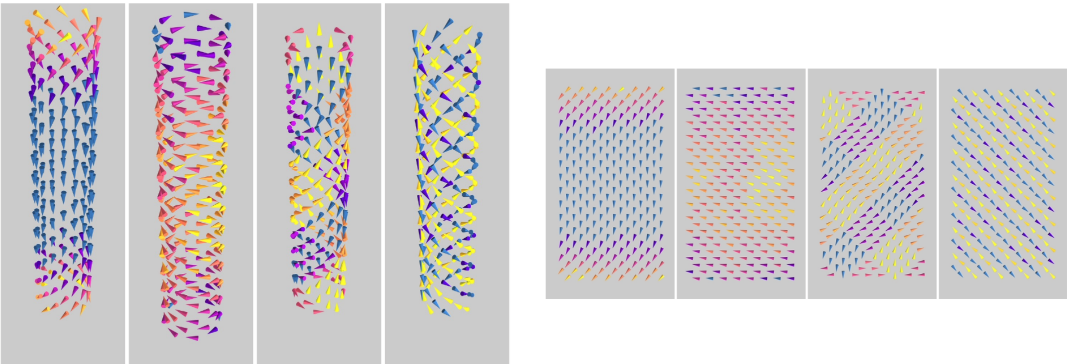

FIG. 5: 8×29, ZZ, $\gamma = 0.40$, $\gamma = 0.75$, $\gamma = 4.00$, $\gamma = 7.00$.

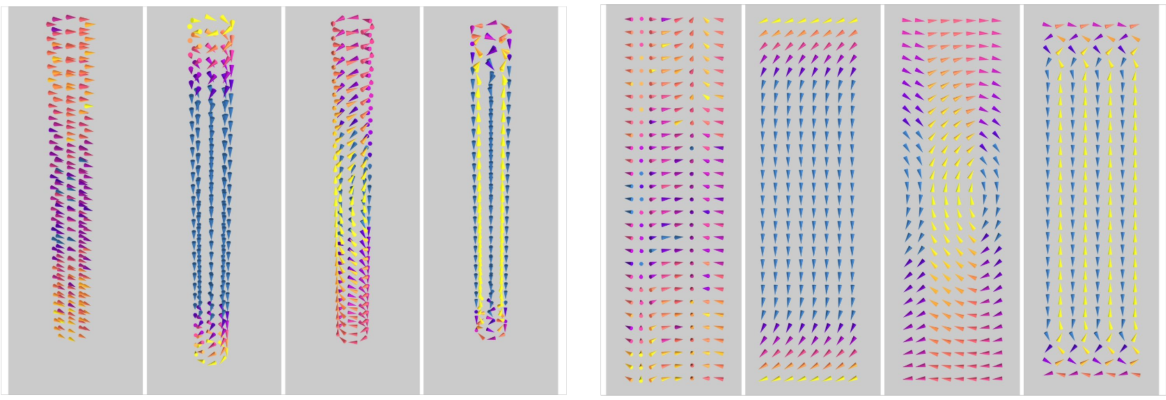

FIG. 6: 8×29, AA, $\gamma = 0.00$, $\gamma = 1.00$, $\gamma = 2.10$, $\gamma = 9.00$.

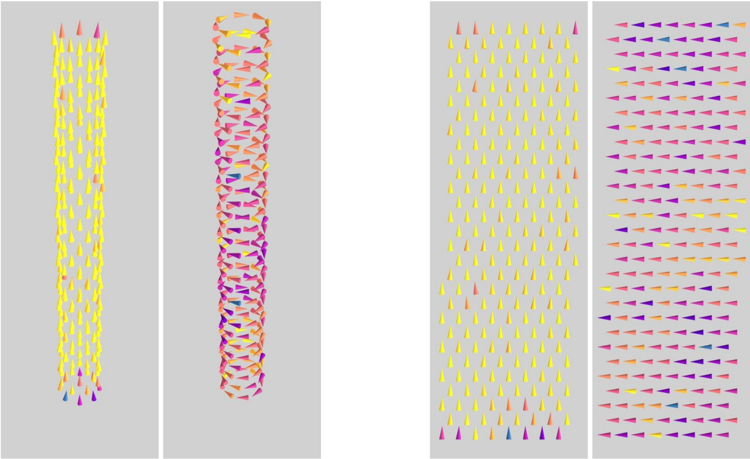

FIG. 7: 8×29, AB, $\gamma = 0.10$, $\gamma = 2.10$.

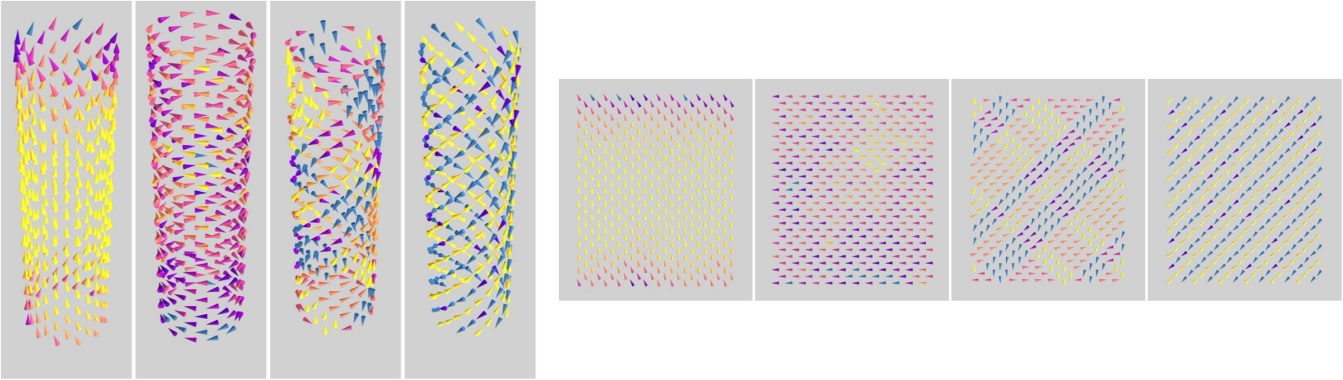

FIG. 8: 12×44, ZZ, $\gamma = 0.15$, $\gamma = 0.29$, $\gamma = 5.50$, $\gamma = 8.00$.

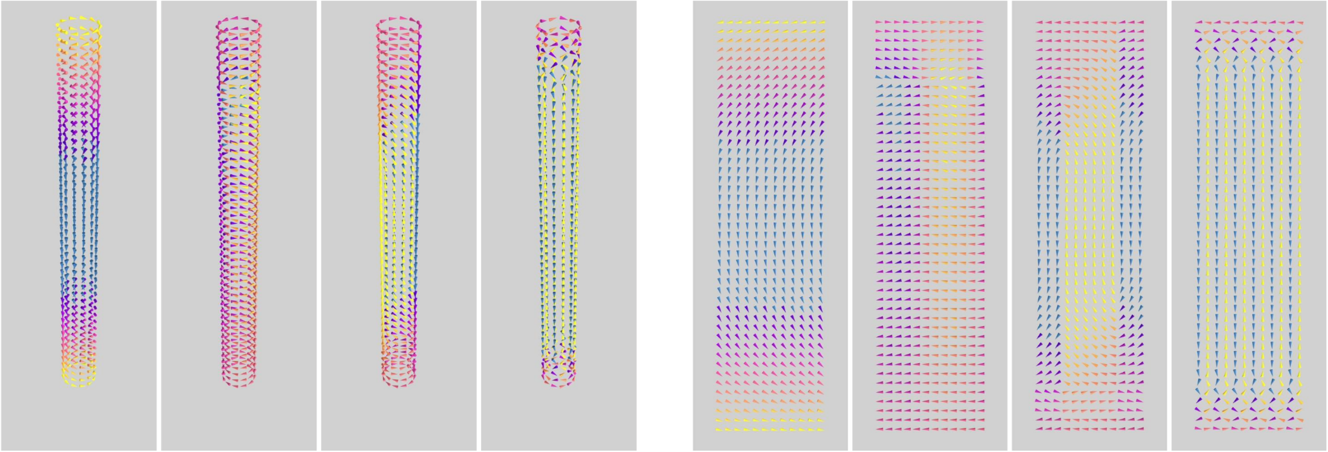

FIG. 9: 12×44, AA, $\gamma = 1.50$, $\gamma = 2.00$, $\gamma = 4.50$, $\gamma = 8.00$.

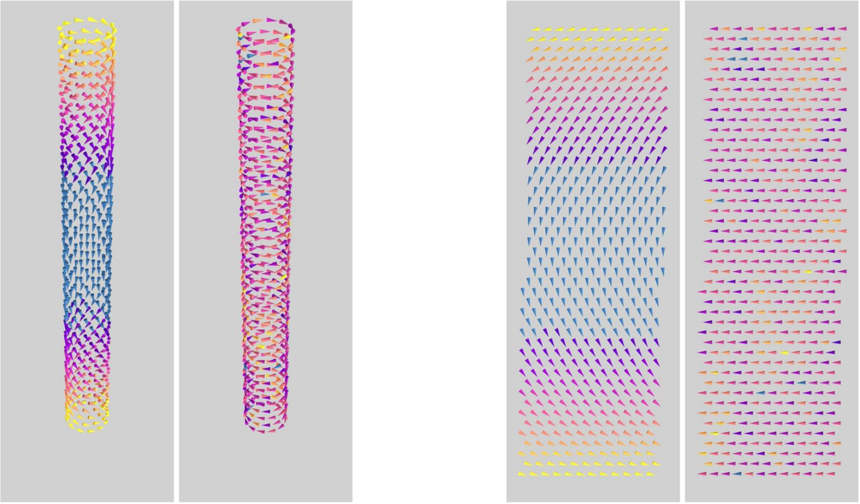

FIG. 10: 12×44, AB, $\gamma = 1.45$, $\gamma = 1.55$.

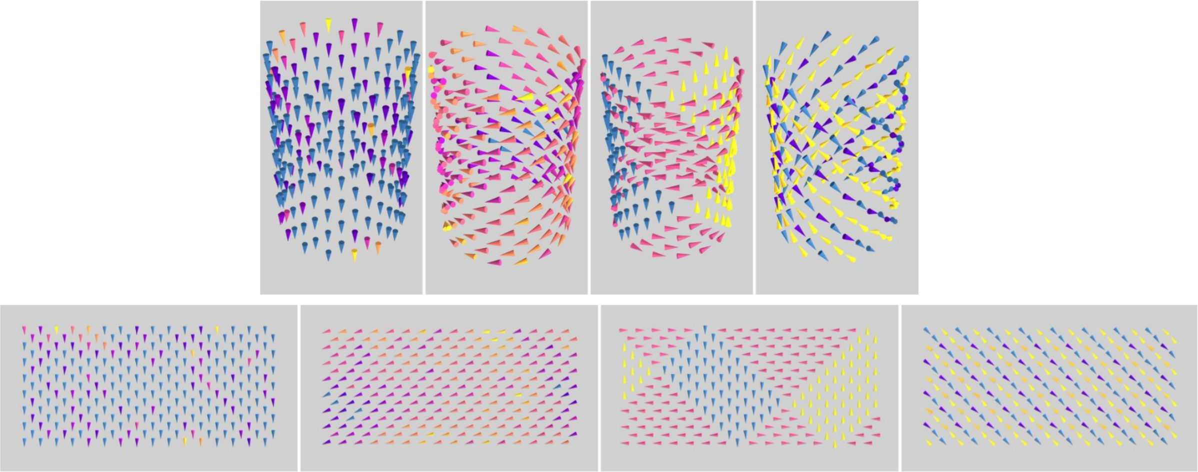

FIG. 11: 16×15, ZZ, $\gamma = 0.04$, $\gamma = 0.64$, $\gamma = 5.00$, $\gamma = 8.50$.

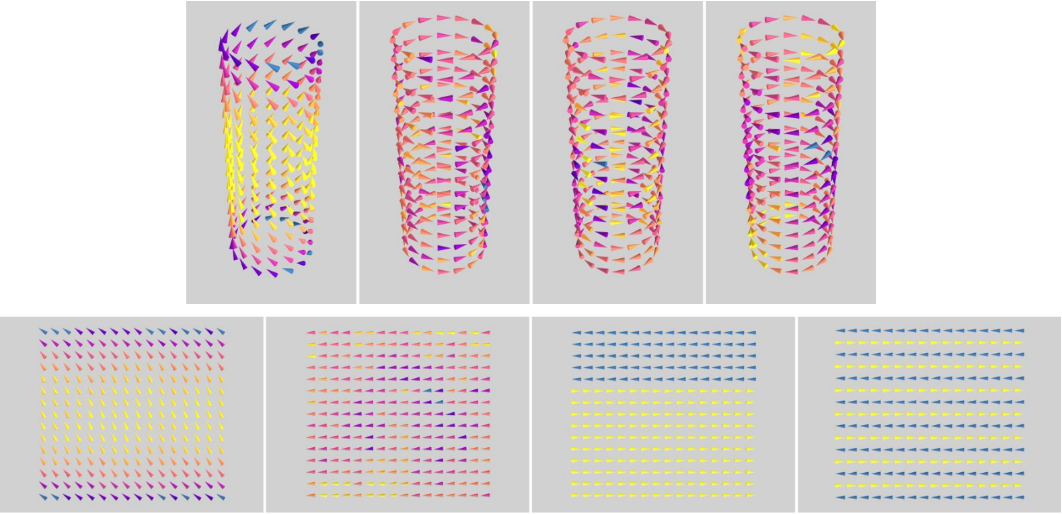

FIG. 12: 16×15, AA, $\gamma = 0.14$, $\gamma = 0.18$, $\gamma = 2.50$, $\gamma = 8.00$.

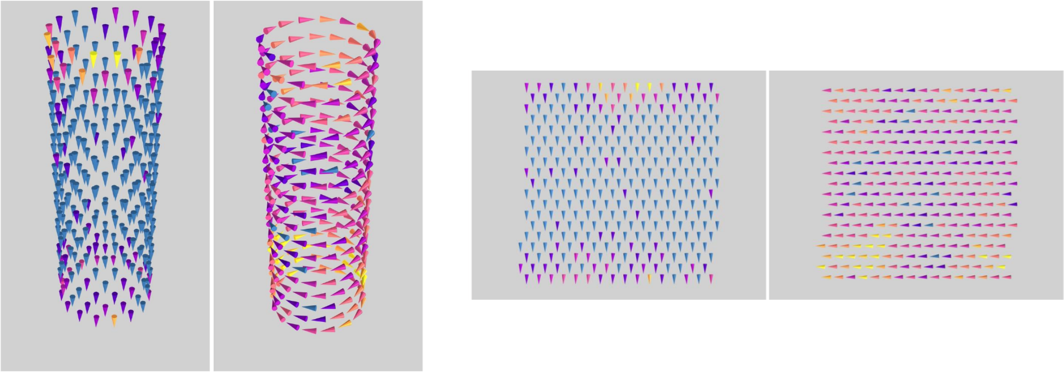

FIG. 13: 16×15, AB, $\gamma = 0.10$, $\gamma = 0.26$.

3. Results with radial anisotropy

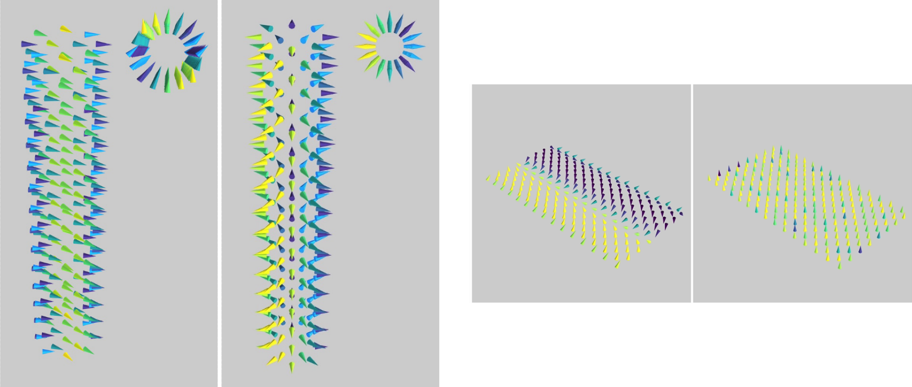

FIG. 14: 8×29, ZZ, $J = 1, g = 0$, $K = 1.00$, $K = 1.50$.

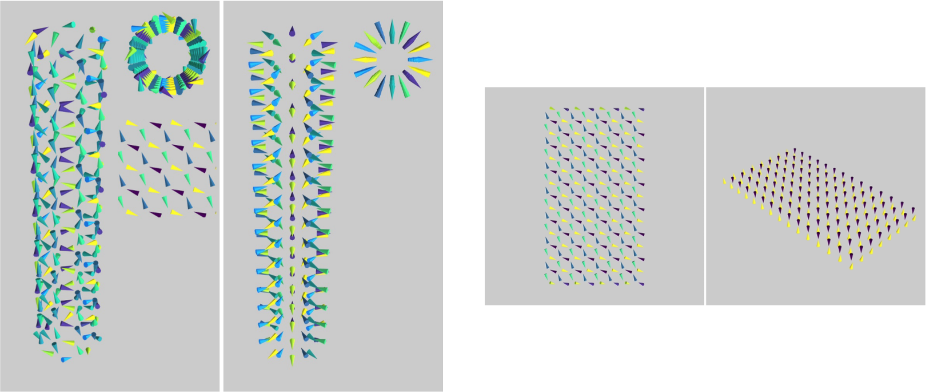

FIG. 15: 8×29, ZZ, $J = 0, g = 1$, $K = 2.00$, $K = 3.00$.

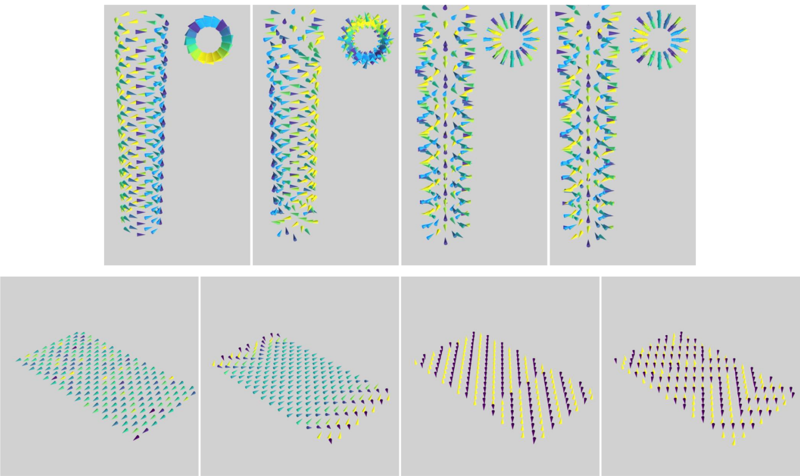

FIG. 16: 8×29, ZZ, $J = 1, g = 1$, $K = 0.00$, $K = 7.00$, $K = 7.50$, $K = 8.00$.

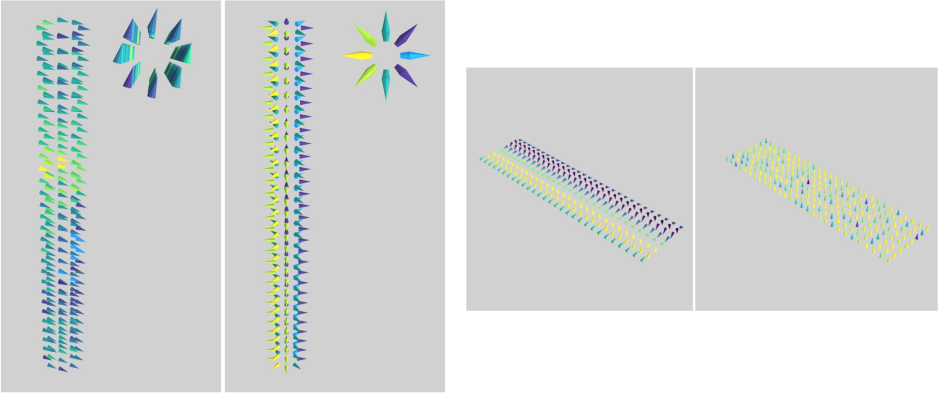

FIG. 17: 8×29, AA, $J = 1, g = 0$, $K = 0.00$, $K = 3.00$.

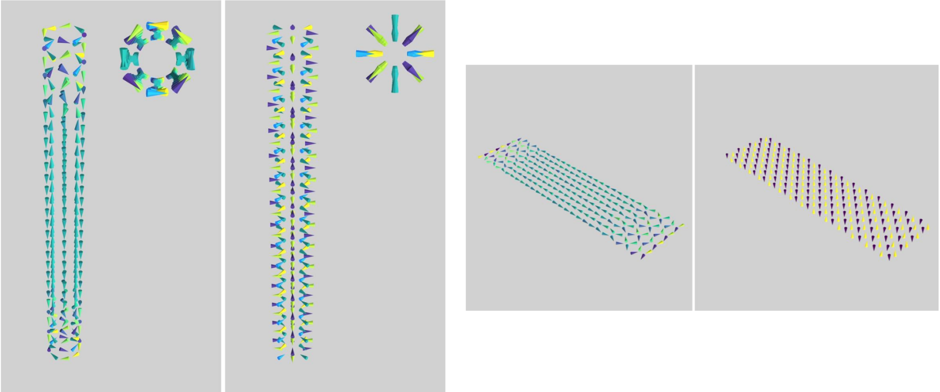

FIG. 18: 8×29, AA, $J = 0, g = 1$, $K = 0.00$, $K = 2.50$.

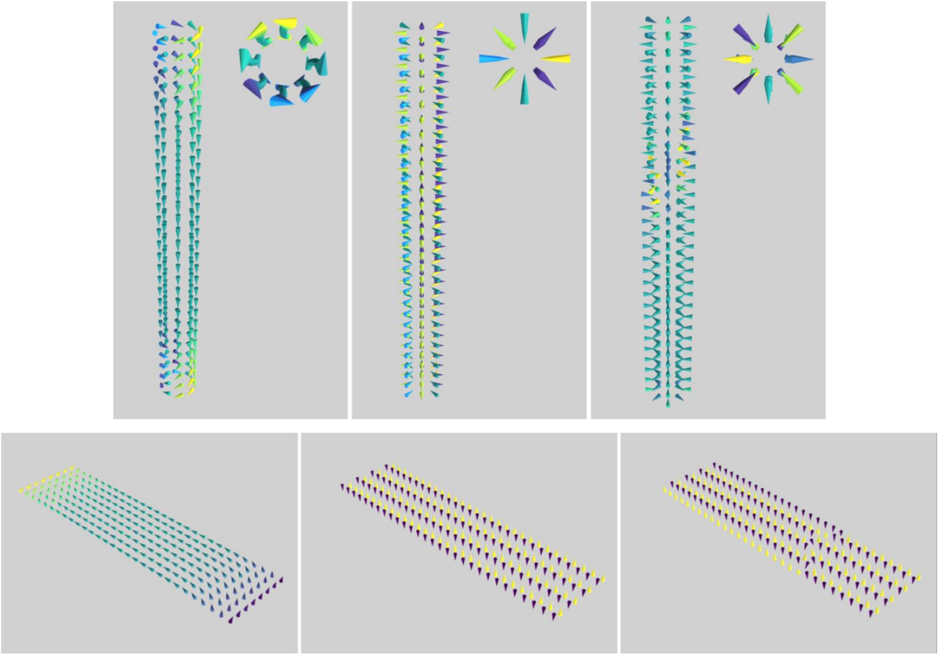

FIG. 19: 8×29, AA, $J = 1, g = 1$, $K = 0.00$, $K = 6.70$, $K = 7.00$.

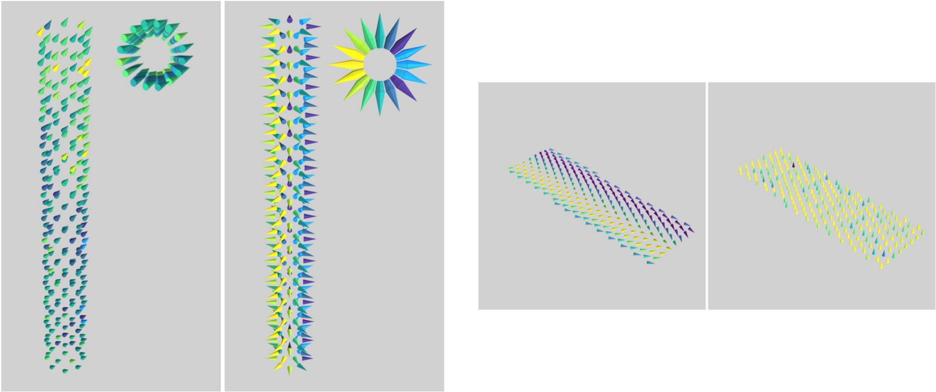

FIG. 20: 8×29, AB, $J = 1, g = 0$, $K = 0.00$, $K = 4.00$.

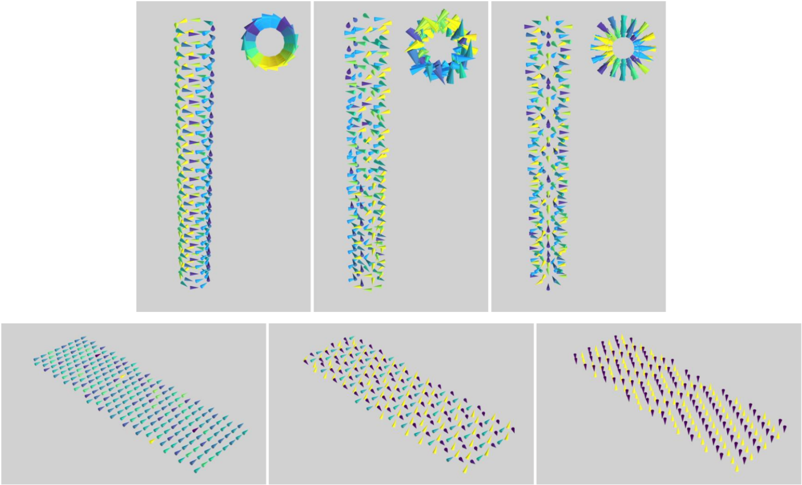

FIG. 21: 8×29, AB, $J = 0, g = 1$, $K = 2.00$, $K = 3.40$, $K = 4.00$.

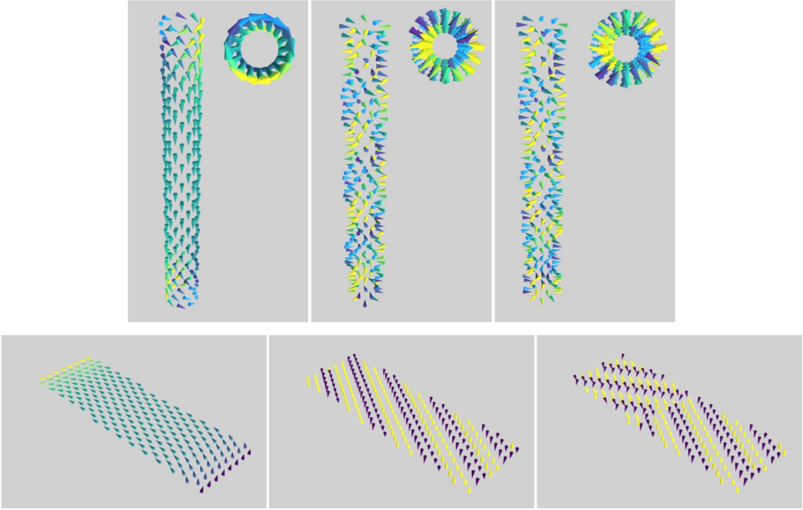

FIG. 22: 8×29, AB, $J = 1, g = 1$, $K = 0.00$, $K = 9.60$, $K = 9.80$.